


ORIGINAL ARTICLE

Open Access



Three-dimensional modeling of moisture transport in wood using near-infrared hyperspectral imaging and X-ray computed tomography in conjunction with finite element analysis

Wenpeng Zeng¹, Takaaki Fujimoto², Tetsuya Inagaki¹, Satoru Tsuchikawa¹ and Te Ma^{1*} 

Abstract

In past studies, finite element analysis (FEA) methods have been used to simulate the thermal and moisture coupling of wood. However, challenges remain in achieving high-quality three-dimensional (3D) simulations, mainly because of the heterogeneous and complex structure of wood and its difficult-to-detect internal structure, which makes modeling challenging, in addition to the lack of robust experimental techniques to validate simulation results. In this study, the FEA simulation model was refined by combining X-ray computed tomography (CT) and near-infrared hyperspectral imaging (NIR-HSI). CT was used to probe the 3D density of wood, and a novel FEA tetrahedral mesh was constructed based on the results. The NIR-HSI method visualizes the moisture distribution during adsorption and desorption inside the wood. This result is then used to adjust the parameters of the FEA simulation model and as a reference value to evaluate the simulation results. The visualization and simulation results fit well with the theoretical properties. The simulation results can more accurately reflect the spatial distribution and transfer trend of wood moisture at different points in time. Therefore, the CT and NIR-HSI-based 3D heat and moisture-coupled FEA model of wood proposed in this study can be used as a basis for optimizing drying parameters to provide high-quality wood.

Keywords Heat and mass transfer, Near-infrared hyper-spectral imaging, Computed tomography, Finite element analysis

Introduction

Wood is classified as a type of naturally occurring macromolecular biomass material. Because of its environmental friendliness and high specific strength, it is widely

used in building materials. However, wood still has some limitations in practical use. The hygroscopic phenomenon always occurs during the use of wood owing to its porous anisotropic structure. This phenomenon primarily depends on the ambient relative humidity (RH), temperature, wood density, and current wood moisture content (MC). Moisture movement affects the physical properties of materials, including their strength, stiffness, and corrosion resistance [1]. Thus, it is crucial to study and simulate the moisture transport characteristics in wood, which can predict the water distribution in the wood over time and provide appropriate protection

*Correspondence:

Te Ma

mate@agr.nagoya-u.ac.jp

¹ Graduate School of Bioagricultural Sciences, Nagoya University, Furo-cho, Chikusa-ku, Nagoya 464-8601, Japan

² Faculty of Agriculture, Tottori University, 4-101 Koyamacho-minami, Tottori 680-8553, Japan



© The Author(s) 2024. **Open Access** This article is licensed under a Creative Commons Attribution 4.0 International License, which permits use, sharing, adaptation, distribution and reproduction in any medium or format, as long as you give appropriate credit to the original author(s) and the source, provide a link to the Creative Commons licence, and indicate if changes were made. The images or other third party material in this article are included in the article's Creative Commons licence, unless indicated otherwise in a credit line to the material. If material is not included in the article's Creative Commons licence and your intended use is not permitted by statutory regulation or exceeds the permitted use, you will need to obtain permission directly from the copyright holder. To view a copy of this licence, visit <http://creativecommons.org/licenses/by/4.0/>.

and repair based on this information to produce durable wooden structures.

Finite Element Analysis (FEA) is a computerized numerical technique for simulating complex physical phenomena. It involves dividing a physical system into finite, interconnected elements to evaluate the behavior of the system under various conditions. Numerous wood moisture-related studies have been conducted regarding this technology. Moisture migration in wood is typically regarded as a thermal mass transfer process that can be calculated by coupling the heat (i.e., Fourier's law) and moisture (i.e., Fick's law) fields. Initially, Erikson et al. [2] performed a two-dimensional (2D) simulation of the transfer of moisture in panels under kiln-drying conditions, considering only the macroscopic level of wood. Gu et al. [3] optimized the model by considering the effect of wood density and MC on thermal conductivity. Zhu et al. [4] artificially considered the microscopic porous structure of wood and introduced gas pressure as a driving force to achieve a 3D-level simulation of wood moisture. Varnier et al. [5] focused on parametric modeling to integrate temperature into the permeability correction. Past studies have demonstrated that as computer technology advances, the FEA of wood moisture is becoming increasingly 3D and refined. However, high-precision 3D simulations of moisture transport in wood remain difficult to achieve. This is mainly because of the heterogeneity and anisotropy of the structure of wood, making it difficult to accurately model and set property parameters. In addition, there is a lack of scientific experimental characterization techniques to support and validate the model. However, this situation can be improved through the application of advanced characterization techniques.

Near-infrared (NIR) spectroscopy is a technique that employs the NIR region of the electromagnetic spectrum, typically between 780 nm and 2500 nm. NIR spectroscopy is distinguished by its reliance on overtones and combination bands of molecular vibrations to determine the chemical composition of a sample. Because the NIR region is not as strongly absorbed as the mid-infrared region, this technique is ideal for probing bulk samples without necessitating extensive sample preparation. At present, NIR has numerous applications. This method is notably applicable to organic compounds such as food [6], pharmaceuticals [7], and agricultural products [8]. At the same time, it has a long-term outlook within the wood industry. NIR permits non-destructive testing (NDT) of the physical and chemical properties of wood in real time. For instance, NIR can be used to estimate the lignin and cellulose content of wood, which is critical for assessing its suitability for specific applications [9]. Similarly, MC—a crucial factor in determining the performance of

wood—can be rapidly and accurately gauged with NIR [10], reducing reliance on time-consuming traditional methods. Therefore, NIR spectroscopy is increasingly becoming an indispensable instrument for the modern wood industry.

Near-infrared hyperspectral imaging (NIR-HSI) is an advanced technology that integrates spatial imaging with traditional NIR spectroscopy. It captures both spatial (x, y coordinates) and spectral (wavelength-dependent) information from a sample, thereby providing a detailed "hyperspectral cube" where each pixel contains a full NIR spectrum. This provides valuable insights into the intra-sample heterogeneity and distribution of wood properties such as density, MC, and microfibril angle [11].

X-ray computed tomography (CT) is an NDT technique that provides a comprehensive analysis of an object's internal and external structures. Using X-rays, the method generates a series of 2D cross-sectional images by scanning the object from different angles. These 2D images are then reconstructed into a 3D model, providing a comprehensive view of the internal features of the object without requiring any physical disassembly or destruction. This technology is extensively used in various industries for quality control, failure analysis, and product development. For instance, it enables the detection of internal defects in manufactured components, such as inclusions, porosity, and cracks, that traditional surface inspection techniques may overlook [12]. In past research, CT has been used for the non-destructive internal examination of logs and timber. It aids in detecting defects such as knots, cracks, and decay, as well as assessing the internal structure and growth rings [13]. In addition, researchers attempt to use this technology to predict wood density distributions [14].

In our previous research, we validated the feasibility of using NIR-HSI for visualizing the moisture distribution in wood during adsorption and desorption processes. In addition, the heat and mass transfer processes were simulated numerically, and the simulation results showed good agreement with the visualization findings [15]. However, the accuracy of density measurements obtained through NIR-HSI was not high. Moreover, the finite difference method based on a three-dimensional matrix has limitations, including neglecting the complex structure of wood and having lower resolution. We aim to optimize the existing FEA model using NIR-HSI and CT techniques to achieve a more accurate 3D simulation of wood moisture migration during absorption and desorption processes. To achieve this goal, CT was used to obtain the 3D density information of the wood, which was subsequently used as the basis for creating the FEA mesh. Then, the NIR-HSI technique was utilized in conjunction with partial least squares (PLS) regression

analysis to construct MC prediction models and visualize the water motion characteristics of wood of varying lengths during adsorption and desorption. Finally, these data and meshes were incorporated into the FEA model to simulate the internal moisture migration of the wood.

Materials and methods

Sample preparation

The wood sample, a Japanese cypress (*Chamaecyparis obtusa*) sawn timber, was purchased commercially from a local processing company. Its dimensions were 1000 mm in the longitudinal direction (L), 30 mm in the tangential direction (T), and 30 mm in the radial direction (R). The wood timber had been stored indoors for an extended period post-purchase and reached an equilibrium moisture content. All parts of timber were taken from sapwood to minimize the variability of wood properties and appropriately reduce the complexity and computational effort of the model. For density model calibration and MC modeling, 24 cubic samples, a side length of 30 mm, were continuously cut longitudinally from the sawn timber using a bandsaw, which minimizes the variation between samples. Two of the samples were selected as the original sources for the simulation.

Computed tomography (CT) data and spectral data acquisition

The main experimental steps of this study are depicted in Fig. 1. The samples were adjusted in the hygroscopic range to obtain different MCs, resulting in absorption and desorption. This was accomplished using desiccators in which the internal RH was controlled via a chemical method. All samples were divided into two groups: the absorption and desorption groups.

Desiccator A was adjusted to a high RH of approximately 95% by adding water, whereas desiccator B was adjusted to a low RH of approximately 10% by adding P_2O_5 . The desiccators were equipped with thermometers for real-time temperature and humidity monitoring. The samples of the desorption group were placed in desiccator A for 10 days and weighed to confirm condition until equilibrium moisture content was reached. Then, these samples were quickly transferred to desiccator B and periodically removed for testing. The samples were initially scanned using a CT scanner (ScanXmate-L080T/L090T, Comscantecno Co., Ltd., Kanagawa, Japan) at 80 kV voltage and 60 mA intensity. CT scans have 400 projections and an accumulation rate of 2 fps. During this process, the sample was mounted on a carrier stage and rotated while the X-ray planar sensor captured 2D X-ray images. Scanning time for each sample is approximately 3 min. Following this, the samples were rapidly cut with a knife in a direction parallel to the fibers into small wooden pieces with a thickness of approximately 3.75 mm, and their cross-sections were recorded using an NIR-HSI system (Compovision, Sumitomo Electric Industries, Ltd., Osaka, Japan). The system consisted of a hyperspectral camera, halogen lamp light source, and mobile carrier table, with the camera capable of receiving NIR light from 1002 to 2350 nm. The horizontal field of view was manually adjusted to 40 mm. The sample was positioned on a moving slider, and the spectral data were scanned line by line with an exposure time of 4.5 ms (200 fps). In addition, samples were weighed before and after image capturing. Then, all samples were fully dried ($103\text{ }^\circ\text{C}$, 48 h), and the total dry weight was determined for MC calculation. For the absorption group, the same experiment was conducted, except that desiccators A and B were replaced in reverse order.

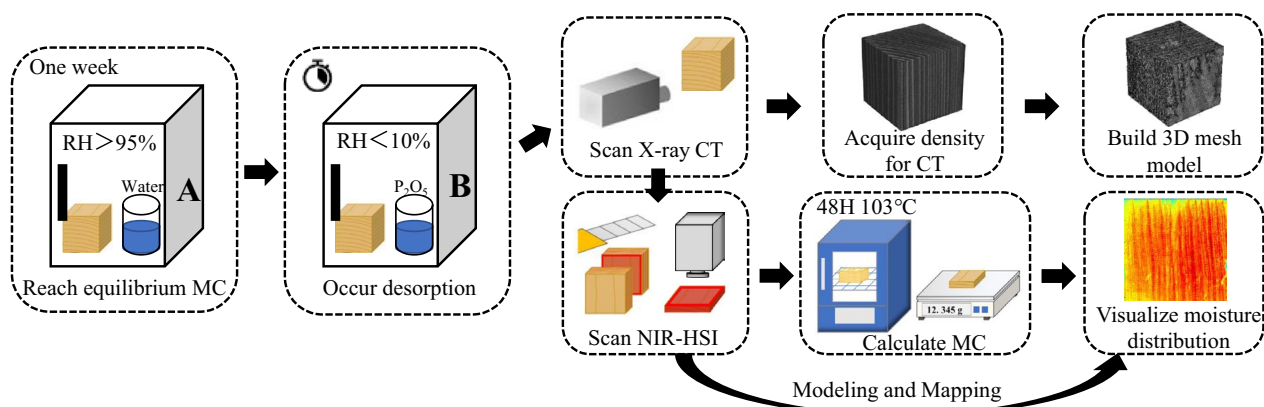


Fig. 1 Experimental flowchart for the desorption process

Computed tomography (CT)-based density prediction model building

During a CT scan, X-rays pass through wood and experience varying degrees of attenuation [16]. This process conforms to Beer's law and can be expressed by Eq. (1).

$$I = I_0 \exp[-l(\mu_1 + \mu_2 + \dots + \mu_i)] \quad (1)$$

where I_0 is the intensity of the ray after attenuation by the object, I the sum of counts detected after attenuation by the object; μ_i the attenuation of the ray through different substances; and l the length of rays passing through each volume element of the object.

To better quantify this attenuation, the CT values (HU) of various regions can be obtained by Eq. (2) and the X-ray attenuation coefficient of water. This is also the most fundamental element of CT images.

$$\text{CT value} = \frac{\mu - \mu_{\text{water}}}{\mu_{\text{water}}} \times 1000 \quad (2)$$

μ_{water} is the linear attenuation coefficient of water and μ the linear absorption coefficient of the detected material. The scale linearly correlates with the actual density: higher CT values represent denser materials. The CT values of dry wood are generally between -800 and -200 HU [17].

Past studies have shown a strong linear relationship between CT values and wood density [18]. Using the measured weight and volume, the average density of the sample was calculated. The acquired CT file was processed by MATLAB (The Mathworks Inc., Natick, MA USA) to eliminate edge noise, reconstruct the 3D representation, and calculate the average CT value for each sample. Linear regression was used to model the relationship between average density and CT value. The established model was applied to each voxel in the 3D representation to accurately map the spatial distribution of wood density.

CT-based 3D FEA mesh creation

CT can accurately measure the size of samples, detect their internal structure, and distinguish between areas of varying densities. The CT model used in this study had a spatial resolution of up to $61.528 \mu\text{m}$. This information is required to create precise FEA mesh information. Figure 2 illustrates the mesh generation process.

First, a threshold segmentation of the original CT 3D representation was performed to distinguish between the earlywood and latewood regions, and then dilation was used to remove noise. This step can reduce the complexity and computational time of the FEA by eliminating unnecessary details. In contrast, segmentation assists in assigning these different properties to the corresponding regions of the FEA model, leading to more accurate simulations.

Based on the Computational Geometry Algorithms Library (CGAL) [19], which helps us create polygons and convex packets and provides Delaunay triangulation mesh generation algorithms, the junction plane between earlywood and latewood was extracted. Then, these planes were automatically subdivided into triangular meshes based on the voxel resolution, and the mesh was further refined at the density set. Using the iso2mesh [20] toolkit, topological defects and isolated points that appeared during the automatic mesh generation process were removed.

Based on an open triangular planar mesh, a square matching the sample dimensions was added to the volume bounding box to obtain multiple closed regions. Invoking the Tetgen 3D mesh generator [21] resulted in the generation of tetrahedral meshes with different densities in various regions, with the density ratio of the earlywood and latewood meshes set to 2:3, which is the same as their average density ratio. The generated meshes were imported into COMSOL (COMSOL Multiphysics® v. 6.1. www.comsol.com. COMSOL AB, Stockholm, Sweden.), statistics of relevant parameters were calculated, and the meshes were used for subsequent finite element calculations.

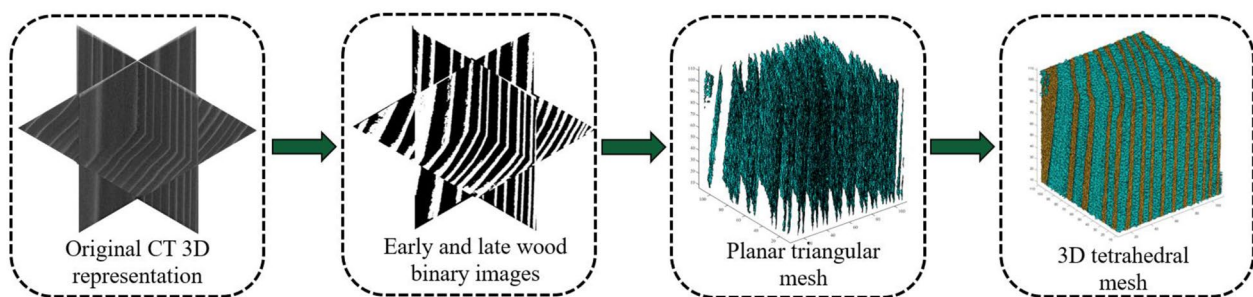


Fig. 2 Flowchart of the mesh generation process

Moisture content calibration model construction using partial least squares (PLS) regression analysis

Under the same conditions as the NIR-HSI scan, a white reference image was generated by scanning a white BaSO₄ plate, and a black reference image was generated by turning off the light source and covering the lens with a lens cap. The original data were corrected by Eq. (3).

$$R_{\lambda,n} = \frac{S_{\lambda,n} - D_{\lambda,n}}{B_{\lambda,n} - D_{\lambda,n}}, \quad (3)$$

where S is the sample data, B is the white plate, D is the black plate, λ represents the different wavelengths, and n represents the position of the pixel.

The five points in the center and on the edges of the corrected hyperspectral image were averaged to represent the spectral information of each slice. The sample MC reference values derived from the weighing method were used to calibrate the NIR mean spectra acquired from each sample using PLS regression analysis. PLS is a regression technique for modeling the relationships between input and output variables using latent variables. PLS reduces dimensionality, mitigates multicollinearity, and maximizes covariance. In NIR spectroscopy, PLS facilitates the management of large, highly collinear datasets, enabling the accurate prediction of concentrations or physical properties. It enables optimal utilization of spectral information, which improves the interpretation of complex, multivariate data. During the development of the model, a random selection of 70% of the total collected data served as the calibration set, while the remaining 30% was set aside as the testing set. The spectral baseline shifts, primarily caused by light scattering, were rectified using standard normal variate (SNV) spectral pre-processing methods. To determine the optimal number of latent variables (LVs), the leave-one-out cross-validation technique was employed. The effectiveness of the established calibration model was assessed through the determination coefficients (R^2) and the root mean square error (RMSE).

In the obtained NIR-HSI data, the spectrum of each pixel was subjected to identical pre-treatments and subsequently to the PLS predictive model to produce MC mapping outcomes.

Wood moisture transport finite element analysis (FEA) simulation

Mathematical formulation and physical field setting

Fourier's law and Fick's law are used to explain the heat-moisture coupling phenomenon in the wood below fiber saturation point (FSP), which mainly includes the flow of heat and the variation of the humidity field. [5] In this section, the mathematical equations of the model are briefly described once more,

and the physical fields and parameters are explained in detail to illustrate how they are set.

Constitutive law of heat transfer The transfer of thermal field in the wood below the FSP can be attributed to the interplay between temperature gradients and vapor pressure differences. In particular, the vapor pressure difference causes fluctuations in the latent heat of adsorption.

Mathematically, the heat transfer mechanism is captured as follows:

$$(\rho_h \cdot C_h) \cdot \frac{\partial T}{\partial t} = \vec{\nabla} (\lambda(w) \cdot \vec{\nabla} T) + H_s \cdot \vec{\nabla} (\delta \cdot \vec{\nabla} (RH \cdot p_{vs})) \quad (4)$$

where ρ_h is the wet density of the wood and computed as follows:

$$\rho_h = \rho_{anh} \cdot (1 + w) \quad (5)$$

where ρ_{anh} represents the absolute dry wood density.

C_h is the wet wood heat capacity, and is provided by the following formula:

$$C_h = \frac{C_{anh} + w \cdot C_w}{1 + w} \text{ with } C_w = 4.18 \text{kJ} \cdot \text{kg}^{-1} \cdot \text{K}^{-1} \quad (6)$$

where C_{anh} is the absolute dry wood heat capacity and C_w the universally accepted heat capacity of water.

Considering the heat caused by the temperature gradient, $\lambda(w)$ serves as the thermal conductivity of the wet material. The final part of the equation encapsulates the heat introduced by the latent heat of adsorption during vapor movement. Here, H_s denotes the heat sorption and p_{vs} represents the saturated vapor pressure. The internal vapor pressure of wood is determined by multiplying the saturation vapor pressure by RH. The heat flow is directly proportional to vapor permeability δ .

The heat sorption H_s is an optimized representation of the latent heat L , factoring in the heat ΔH_s released by the water bound to the cellulose. This heat, termed the enthalpy of adsorption, is computed as follows:

$$H_s = L - \Delta H_s \quad (7)$$

$$\Delta H_s = A \cdot \ln\left(\frac{w}{w_s}\right) \quad (8)$$

where w_s denotes the MC of wood at the saturation point of the fibers, and A is a water capacity parameter.

Constitutive law of mass transfer For the mass transfer process, the movement of water, driven by gradients in both RH and saturation water vapor pressure, is key. The following equation captures this mechanism:

$$\left(\rho_{anh} \cdot \frac{\partial w}{\partial RH}\right) \cdot \frac{\partial RH}{\partial t} = \vec{\nabla}(\delta^* \cdot p_{vs} \cdot \vec{\nabla} RH) + \vec{\nabla}(\delta \cdot RH \cdot \vec{\nabla} p_{vs}) \tag{9}$$

where δ^* is the apparent permeability, an important factor in water movement that focuses on liquid water movement as opposed to δ :

$$\delta^* = \delta_0 \cdot \exp\left(-\frac{E_a}{R \cdot T}\right). \tag{10}$$

The activation energy E_a is vital in this setup. It is determined as follows:

$$E_a = H_s - (C_{p_v} \cdot T). \tag{11}$$

Incorporating the latent heat energy of adsorption into the overall energy.

Mesh and boundary condition setting

The mesh and boundary conditions are shown in Fig. 3. The mesh was derived from the FEA mesh constructed based on CT. The five upper surfaces of the model were convected with air for heat and moisture exchange, whereas the bottom surface perpendicular to the L direction was configured as an insulated surface without heat and water vapor exchange because it is in direct contact with the platform.

The heat and moisture transfer on the convective exchange surface is given by Eqs. (12–13):

$$\lambda \cdot \frac{\partial T}{\partial x} = h_T \cdot (T_{amb} - T_{surf}) \tag{12}$$

$$\delta \cdot \frac{\partial RH}{\partial x} = h_w \cdot (RH_{amb} - RH_{surf}) \tag{13}$$

where T_{amb} and RH_{amb} denote the ambient temperature and RH, both of which are obtained from temperature

and humidity meter measurements in the desiccators, which are considered homogeneous sources. T_{surf} and RH_{surf} represent the temperature and humidity of the sample surface, which are derived from the initial setting and subsequent derived values. h_T and h_w indicate the temperature and humidity convective exchange coefficients, respectively.

Finite element analysis (FEA) simulation model construction and parameter setting

The entirety of the model was constructed using the COMSOL 6.1 software environment. The coefficient-type partial differential equation module was utilized, and the solver was configured as a transient solver with a 1-min time step. The initial density and MC in the model were derived from the CT and NIR-HSI estimates, respectively. Other parameters were set based on a previous study by Ma et al. [15]. In addition, the anisotropy of the wood structure must be considered, and correction factors must be applied to the diffusion coefficients and surface radiation coefficient in the geometric direction. The simulation results were compared with the MC mapping results obtained by the NIR-HSI method, and the correction coefficients were manually adjusted. Through multiple simulations, the best-fit result was obtained with the following parameter settings:

$$h_w = \begin{pmatrix} 0.5 * h_{wL} & 0 & 0 \\ 0 & 0.7 * h_{wL} & 0 \\ 0 & 0 & h_{wL} \end{pmatrix} \tag{14}$$

$$\delta_d = \begin{pmatrix} 0.4 * \delta_{dL} & 0 & 0 \\ 0 & 0.6 * \delta_{dL} & 0 \\ 0 & 0 & \delta_{dL} \end{pmatrix} \tag{15}$$

$$\delta_a = \begin{pmatrix} 0.08 * \delta_{dL} & 0 & 0 \\ 0 & 0.1 * \delta_{dL} & 0 \\ 0 & 0 & 0.3 * \delta_{dL} \end{pmatrix} \tag{16}$$

where the three rows of the matrix represent the T, R, and L directions of the sample respectively. h_w is humidity convective exchange coefficient. δ_d and δ_a denote the vapor permeability during the absorption and desorption processes, respectively. δ_{dL} is vapour permeability in the L direction during desorption, which set based on a previous study in Mouchot et al. [22]. According to it, the parameters of the anisotropy in the other directions were set by coefficients. This coefficient is also consistent with the common perception of wood structure.

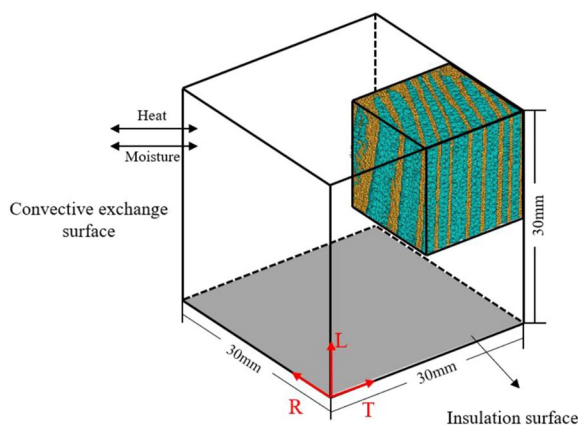


Fig. 3 Geometry, FEA mesh, and boundary conditions settings

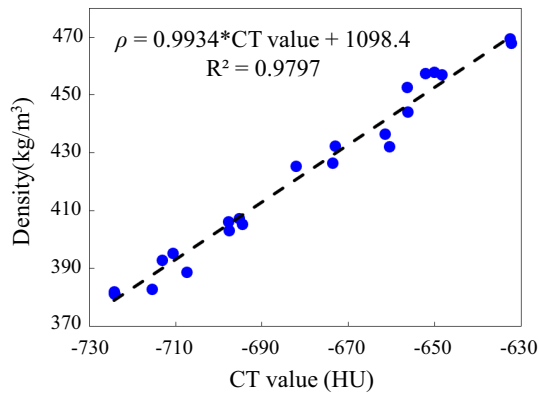


Fig. 4 Linear equation and relationship diagram of wood CT value-density

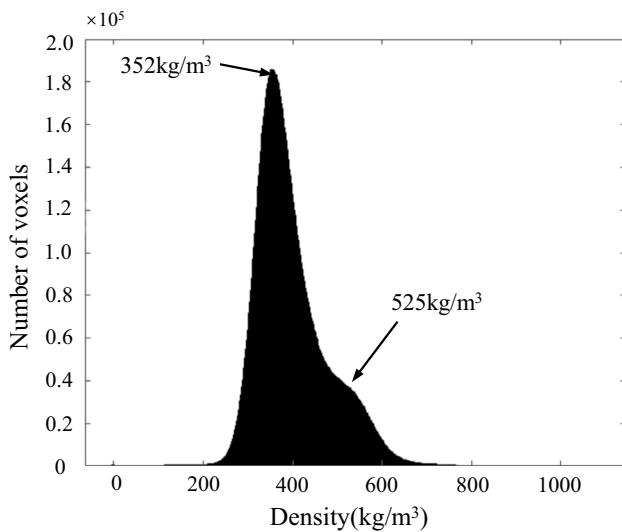


Fig. 5 Distribution of sample voxel density

Result and discussion

The measured wood densities ranged from 380 to 470 kg/m³. CT values fluctuated between -725 HU and

-630 HU. Figure 4 depicts the linear equation model and the relationship diagram that can be derived by linear regression of the average density and the average CT value. There was a significant linear relationship between density and CT values for the 24 wood samples, with the coefficient of determination R^2 exceeding 0.979, which verified the reliability of the model. The range of CT values and modeling accuracy were similar to those of previous studies on softwoods [18].

The model was substituted into each voxel of the 3D CT expression to obtain the sample density distribution. Figure 5 depicts the number of voxels with different densities. The densities were mainly concentrated between 200 and 700 kg/m³. There were two peaks at 352 and 525 kg/m³, which indicated the density concentration of earlywood and latewood, respectively, and the peak height of earlywood was significantly higher than that of latewood, which was consistent with the reality that the proportion of earlywood in the samples was greater than that of latewood.

Figure 6 illustrates the CT-based FEA mesh model of one of the samples, which comprises 774361 nodes, 1861044 triangle meshes, and 4569112 free tetrahedral meshes. The average mesh quality can reach 0.7. It is generally believed that a mesh quality greater than 0.5 does not affect the convergence of FEA calculation results [23]. The mesh density in the earlywood region was significantly lower than that in the latewood region, which better reflected the differences in structure and properties between earlywood and latewood. Because the principle of generating volume meshes by Tetgen is based on the fractal theorem, denser meshes are generated at the earlywood and latewood junctions, which facilitates the description of the strong temperature-moisture gradient changes that occur in this region. In the new mesh, the alterations between earlywood and latewood were visualized, and the mesh density was linked to the actual wood density, which better

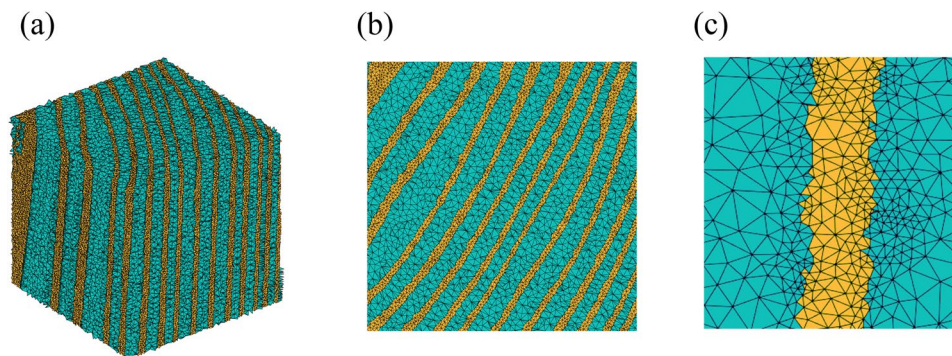


Fig. 6 CT-based FEA mesh. **a** Mesh 3D view; **b** Mesh T-R cross-section view; **c** detailed view of the mesh at the junction of earlywood and latewood

reflected the geometrical and physical properties of the samples compared to the previous mesh [24, 25].

A thermohydrimeter was used to measure temperature and RH in the desiccators in real-time. The temperature fluctuated with day and night, whereas the RH was maintained in a relatively stable state, except for small fluctuations when samples were introduced. This indicates that water and P₂O₅ can effectively control the RH to provide a stable environment for the experiment. The average RH of the high-humidity desiccator reached 94%, whereas the average RH of the low-humidity desiccator reached an average RH of 29%. These data were also used to construct the simulation models.

Figure 7 shows the average spectra of the samples with different MCs; two prominent water-related absorption peaks were observed at 1450 nm and 1930 nm, which originated from the molecular vibrations of O–H [26]. Light absorption at 1930 nm was stronger than that at 1450 nm, which indicated that the long-wave NIR spectrum contained more moisture information. In addition, it could be observed that wood with a higher MC tends to have lower light reflectance in this location.

In the modeling process, the spectra of wavelengths below 1350 nm and above 2050 nm were excluded because of noise. Figure 8 depicts the PLS process outcome, which includes the influence rate of principal components, the RMSE of predictors and reactions, and the PLS regression coefficients. These results indicate that the percentage variance of the average reflectance spectra increased in correlation with the number of latent

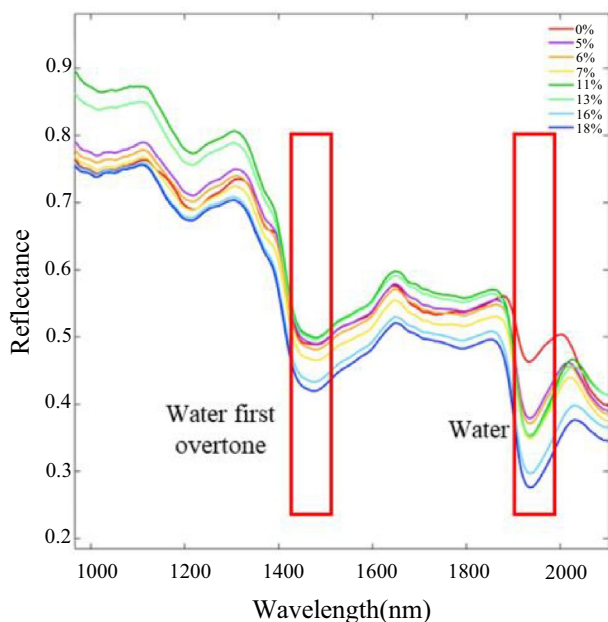


Fig. 7 Averaged NIR spectra of different MCs

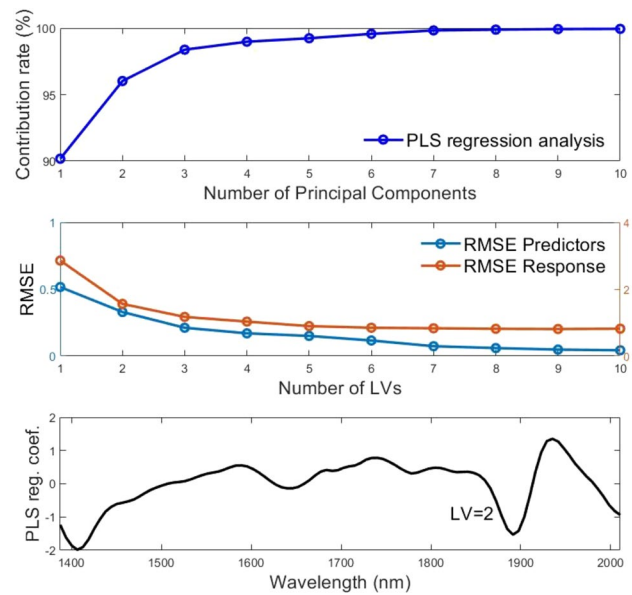


Fig. 8 PLS results. a Contribution rate of the LVs; b RMSE of predictors and response in different LVs; c PLS regression coefficients

variables (LVs). When two LVs were employed, approximately 95% of the variance in the spectral data was justified, indicating that the fluctuations in the NIR spectra were likely because of changes in MC. Furthermore, as the number of LVs increased, the predictor and its associated RMSE showed a decreasing trend. However, an overly reduced RMSE may result in model overfitting. Therefore, two LVs were chosen to enhance the robustness of the PLS model. The regression coefficient diagram exhibits greater absolute values in the vicinity of water-related wavelengths (i.e., 1450 nm and 1930 nm). This signals that the strength of the O–H absorption peak plays a significant role in the model.

Figure 9 shows the accuracy of the predicted model, for which the R^2 and RMSE were 0.89 and 1.69% for the test set, respectively. It is evident that the long-wave NIR–HSI method is robust to quantify MC in the wood below the FSP.

Figure 10 displays the HSI mapping results for the a desorption and b adsorption processes on wood MC distributions. By rearranging the planar results in the R-direction, the MC distributions at the 3D level were obtained. During the desorption process, the moisture distribution was relatively uniform in the initial stage, with the MC on the outside being slightly lower than that on the inside. As desorption proceeded, a large moisture gradient was formed between the surface layer and the interior. Then, when the surface layer attained equilibrium MC, the difference in MC between the interior and exterior decreased over time. This process was consistent

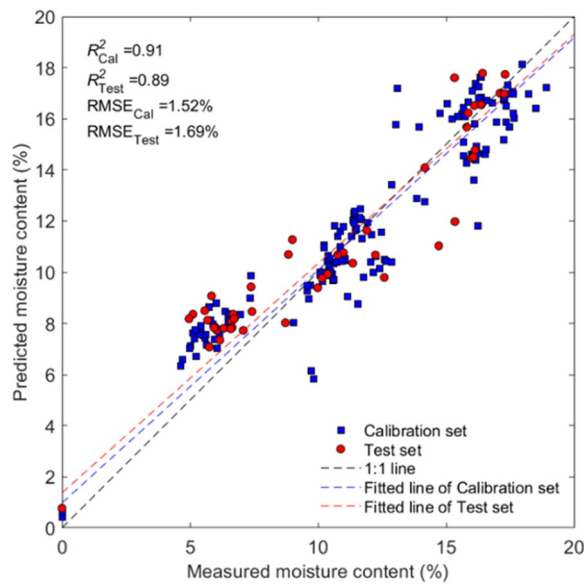


Fig. 9 Scatter plot illustrating the differences between the MC reference values and their predicted values by the NIR-HIS

with the hypothesis that water molecules in the air seek equilibrium with those in wood cell walls [27]. The absorption process was similar to the desorption process; however, the MC changed more gradually. This effect was due to changes in the wood’s microstructure and chemical composition during the initial moisture adjustment, which results in a reduction in the moisture adsorption point of the wood and a lower equilibrium MC [1]; smaller differences between equilibrium and real-time MC ultimately lead to slower reabsorption. In addition, during desorption, rapid surface moisture evaporation coupled with slow internal moisture movement created a

significant moisture gradient between the heart and surface layers [28]. Conversely, during moisture absorption, the process was slower and resulted in a more uniform MC distribution across both surface and interior. Furthermore, the initial MC in the latewood is higher than that in the earlywood (Fig. 11). This could be due to that the latewood cellulose content is slightly higher while the lignin content is slightly lower than in earlywood which facilitates more hydrogen bonding with water molecules [29].

Figure 12 shows the reference and predicted average MC values over time. During desorption and absorption, the simulated and reference values were in good agreement, indicating that the simulation model had good performance in the overall MC simulation. Initially, the rate of change of MC was greater, but as the difference in relative humidity between the interior and exterior decreased, the rate of change slowed and eventually assumed a parabolic form.

To evaluate the spatial accuracy of the model simulations, reference obtained using the weighing method for each slice of wood and FEA predicted values of the average MC along the R direction of the sample slices were compared (Fig. 13). Reference obtained by Oven-dry method of sample slices. In the initial state, the distribution of moisture was not as uniform as expected owing to the complex structure of the wood. During desorption, the MC of the right side was slightly higher than that of the left side because of the denser distribution of latewood on the right side, which had a greater water storage capacity. In the absorption group, the knots in the wood caused a low MC zone on the left side. As desorption and adsorption proceeded, this inhomogeneous moisture distribution was displaced by ordered internal and external moisture gradients, a phenomenon exhibited in both

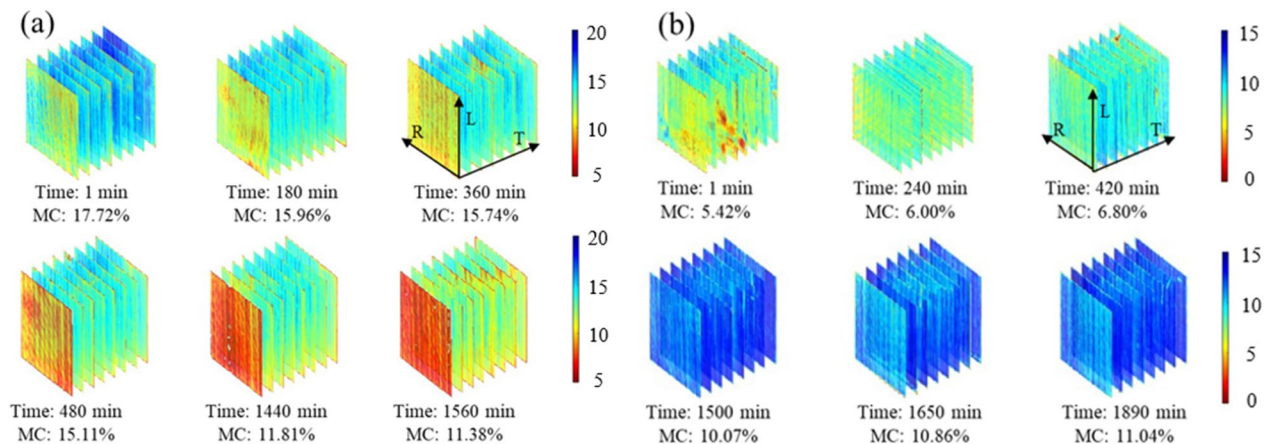


Fig. 10 MC mapping results with samples during the **a** water desorption and **b** adsorption processes under the FSP

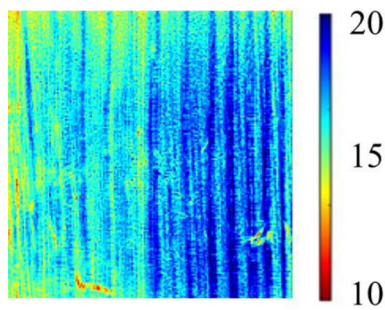


Fig. 11 Middle layer MC mapping result in initial state during desorption process

reference and predicted values and consistent with the theory of moisture absorption in porous materials [30]. Although the trend of the simulated results was similar to that of the reference results, the simulated results were more difficult to fit numerically. On the one hand, this bias originated from the variability of the samples. The samples used to test the reference MC at each stage were similar but distinct (the sample was cut during the hyperspectral scan and was unavailable for subsequent experiments). On the other hand, in this model, the difference in vapor permeability between morning and evening timber was not considered in a significant manner, and this simplification resulted in simulated moisture distributions that always converged to equilibrium more quickly.

To further evaluate the performance of the model in simulating the 3D moisture distribution species, the visualization results obtained from NIR-HSI of the T-L section located in the center of the sample were compared with the predicted results. Figure 14 demonstrates that, in comparison to the previous model, the simulation results better reflect the spatial trend of moisture migration. Because of the introduction of the initial spatial distribution of MC and density, it can be observed in the simulation results that at the beginning of the desorption and absorption of the wood, the moisture distribution was not as homogeneous as expected, but with time,

the moisture distribution gradually exhibited the gradient distribution from the outside to the inside, which was more in line with the previously obtained results. In addition, as a result of the setting of the correlation factors, the moisture moved more rapidly in the L direction than in other directions, and the moisture distribution was relatively uniform during the absorption process. Under the current correlation factor settings, the best fit between the simulated values and the reference values could be achieved. Although experimental verification of the physical significance of the parameter settings is necessary, these values are associated with the effect of the anisotropy of wood microstructure on the hygroscopic properties of wood [31].

It is important to note that the model had some limitations. First, in the simulation results, the bottom had a low MC because of the setting of the insulation boundary. However, in the reference results, moisture exchange with air at the bottom was still observed, which was owing to the porous wood structure [32]. In addition, the model did not perform well in terms of details, and the difference in MC between earlywood and latewood disappeared with increasing simulation time. This was likely because considering only the spatial distribution of densities did not adequately characterize the migration of moisture between earlywood and latewood, and there was room for the mesh density to increase. Taking parameters such as porosity or pore size distribution into account in the model should result in a more reasonable response to the hygroscopic properties of different wood regions [33, 34].

Conclusions

In this study, the 3D properties of the wood (density, MC, and mesh model) were probed using NDT tools such as CT and NIR-HSI. Then, for the first time, these complex non-homogeneous properties were incorporated into the modeling and calculation of wood FEA simulations. The new model had high accuracy in the overall

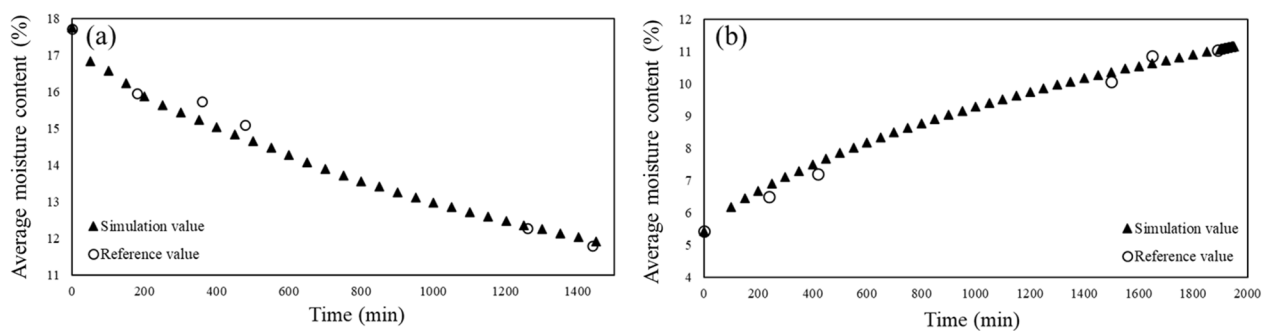


Fig. 12 Reference and simulated values of the average MC of samples at various time periods. **a** Desorption; **b** absorption

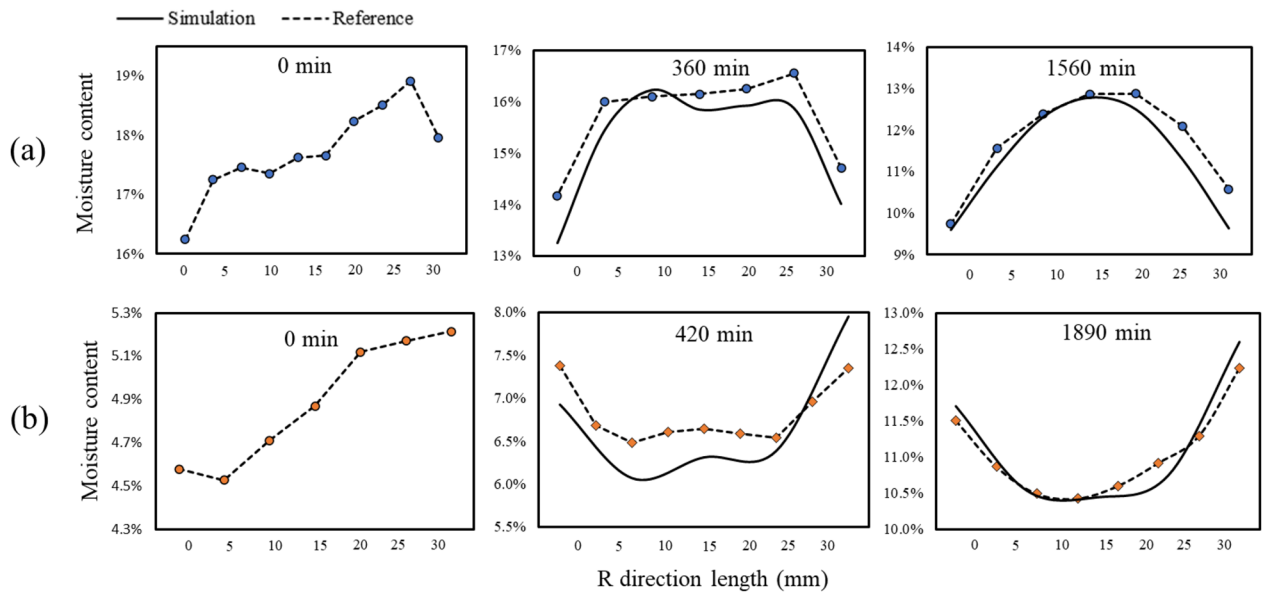


Fig. 13 Reference and simulation average moisture content of the sliced samples arranged diagonally along the sample R direction. **a** Desorption; **b** absorption

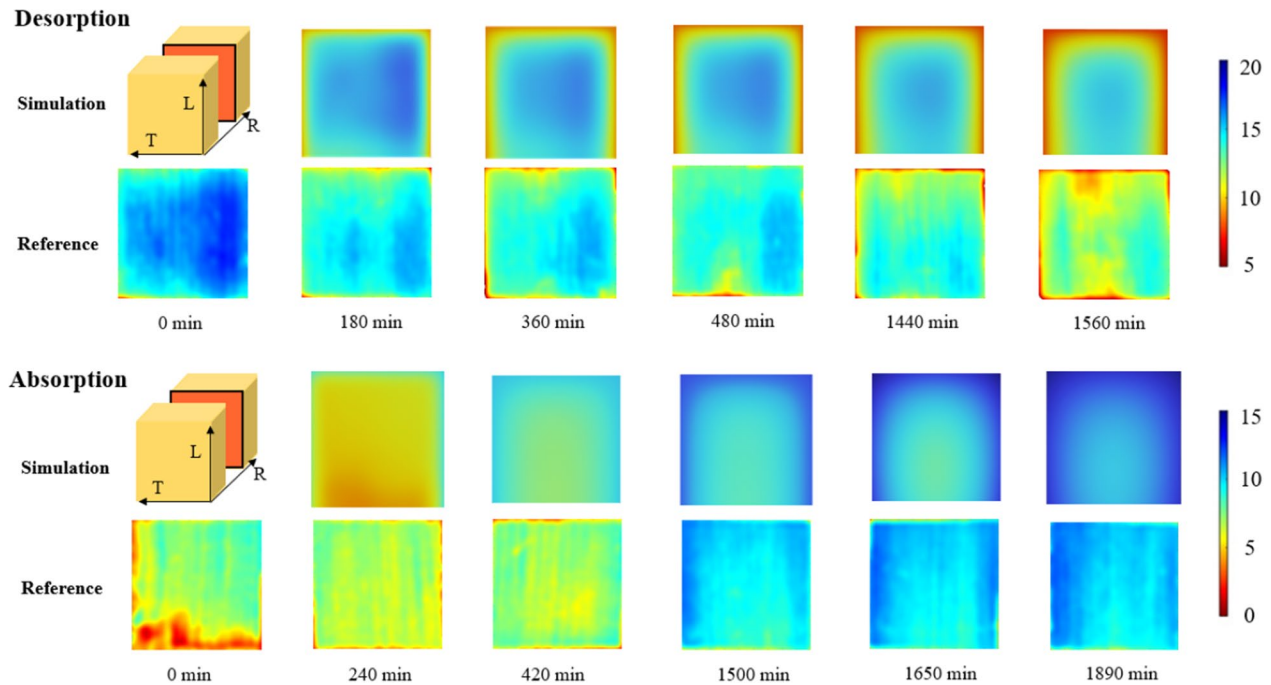


Fig. 14 Reference and simulation comparisons of the internal moisture content distribution of wood

MC simulation and responded to the trend of moisture migration at the 3D level.

There is still substantial room for improvement in the model, including optimizing the boundary conditions, analyzing the influence of wood structure on parameters

such as vapor permeability in greater depth, and achieving a balance between calculation time and calculation accuracy. Overall, despite the limitations, this study illustrates the potential of FEA as a valuable tool for simulating moisture transport in wood. This can greatly improve

our understanding and prediction of moisture-related processes in wood, which is critical for numerous industries that utilize wood. The addition of advanced characterization tools will also allow us to refine the FEA simulation process to achieve an improved outcome.

Abbreviations

| | |
|----------------------|--|
| CT | X-ray computed tomography |
| NIR-HSI | Near-infrared hyperspectral imaging |
| RH | Relative humidity |
| MC | Moisture content |
| NIR | Near-infrared |
| NDT | Non-destructive testing |
| PLS | Partial least squares |
| I_0 | Intensity of the ray after attenuation by the object |
| I | Sum of counts detected after attenuation by the object |
| μ_i | Attenuation of the ray through different substances |
| l | The length of rays passing through each volume element of the object |
| μ_{water} | Linear attenuation coefficient of water |
| μ | Linear absorption coefficient of the detected material |
| CGAL | Computational Geometry Algorithms Library |
| SNV | Standard normal variate |
| LVs | Latent variables |
| R^2 | Determination coefficients |
| RMSE | Root mean square error |
| FSP | Fiber saturation point |
| ρ_h | Wet density of the wood |
| ρ_{anh} | Absolute dry wood density |
| C_h | Wet wood heat capacity |
| C_{anh} | Absolute dry wood heat capacity |
| C_w | Heat capacity of water |
| $\lambda(w)$ | Thermal conductivity of the wet material |
| p_{vs} | Saturated vapor pressure |
| δ | Vapor permeability |
| H_s | Heat sorption |
| L | Latent heat |
| ΔH_s | Heat released by the water bound to the cellulose |
| w_s | MC of wood at the saturation point of the fibers |
| A | Water capacity parameter |
| δ^* | Apparent permeability |
| E_a | Activation energy |
| T_{amb} | Ambient temperature |
| RH_{amb} | Ambient RH |
| T_{surf} | Temperature of the sample surface |
| RH_{surf} | RH of the sample surface |
| h_T | Temperature convective exchange coefficients |
| h_w | Humidity convective exchange coefficients |
| δ_a | Vapor permeability during the absorption |
| δ_d | Vapor permeability during the desorption |

Acknowledgements

Thanks to Dr. Wang Han, Dr. Yuan Jiacheng, and Dr. Li Bin for guiding the authors in data processing. The authors acknowledge the Japan Wood Research Society for providing the Article Processing Charge of this article.

Author contributions

WZ: data curation, formal analysis, validation, writing—original draft preparation. TF: methodology, validation, writing—reviewing and editing. TI: conceptualization, methodology, validation, writing—reviewing and editing. ST: supervision, validation, writing—reviewing and editing, funding acquisition. TM: conceptualization, data curation, validation, writing—original draft preparation, funding acquisition. All authors have read and agreed to the published version of the manuscript.

Funding

This study is supported by JSPS (KAKENHI, No. 22K14926 and 22H02405). This work was supported by The International Exchange Encouragement Award

from the Japan Wood Research Society through JSPS KAKENHI, Grants-in-Aid for Publication of Scientific Research Results (JP 22HP2003).

Availability of data and materials

The datasets used and/or analyzed during the current study are available from the corresponding author on reasonable request.

Declarations

Competing interests

No potential conflict of interest was reported by the authors.

Received: 10 October 2023 Accepted: 28 December 2023

Published online: 26 January 2024

References

- Fredriksson M (2019) On wood–water interactions in the over-hygrosopic moisture range—Mechanisms, methods, and influence of wood modification. *Forests* 10(9):779
- Eriksson J, Ormarsson S, Petersson H (2006) Finite-element analysis of coupled nonlinear heat and moisture transfer in wood. *Num Heat Transf Part A Appl* 50(9):851–864
- Gu, H., & Hunt, J. F. (2007). Two-dimensional finite element heat transfer model of softwood. Part III. Effect of moisture content on thermal conductivity. *Wood Fiber Sci* 159–166.
- Zhu Z, Kaliske M (2011) Modeling of coupled heat, moisture transfer and mechanical deformations of wood during drying process. *Eng Comput* 28(7):802–827
- Varnier M, Sauvat N, Ulmet L, Montero C, Dubois F, Gril J (2020) Influence of temperature in a mass transfer simulation: application to wood. *Wood Sci Technol* 54:943–962
- Cozzolino D (2021) The ability of near infrared (NIR) spectroscopy to predict functional properties in foods: challenges and opportunities. *Molecules* 26(22):6981
- Zhou L, Xu M, Wu Z, Shi X, Qiao Y (2016) PAT: from Western solid dosage forms to Chinese material medica preparations using NIR-CI. *Drug Test Anal* 8(1):71–85
- Zhang J, Liu Z, Pu Y, Wang J, Tang B, Dai L, Chen R et al. (2023) Identification of transgenic agricultural products and foods using nir spectroscopy and hyperspectral imaging: a review. *Processes* 11(3), 651.
- Poke FS, Raymond CA (2006) Predicting extractives, lignin, and cellulose contents using near infrared spectroscopy on solid wood in *Eucalyptus globulus*. *J Wood Chem Technol* 26(2):187–199
- dos Santos LM, Amaral EA, Nieri EM, Costa EVS, Trugilho PF, Calegário N, Hein PRG (2021) Estimating wood moisture by near infrared spectroscopy: Testing acquisition methods and wood surfaces qualities. *Wood Mat Sci Eng* 16(5):336–343
- Yang H, Ni J, Chen C, Chen C (2023) Weathering assessment approach for building sandstone using hyperspectral imaging technique. *Heritage Science* 11(1):1–18
- Hernandez-Contreras A, Ruiz-Huerta L, Caballero-Ruiz A, Moock V, Siller HR (2020) Extended CT void analysis in FDM additive manufacturing components. *Materials* 13(17):3831
- Yang X, Gao Y, Zhao Z, Ge Z, Liu X, Zhou Y (2022) Detection and analysis of an eave purlin of the timber building eroded by carpenter bees based on computed tomography. *BioResources* 17(2):2443
- Yan, D., & Zhang, J. (2009, October). Five-layer realistic head model based on inhomogeneous and anisotropic conductivity distribution of different tissues. In *MIPPR 2009: Medical Imaging, Parallel Processing of Images, and Optimization Techniques* (Vol. 7497, pp. 633–639). SPIE.
- Ma T, Morita G, Inagaki T, Tsuchikawa S (2022) Experimental study and three-dimensional modeling of moisture transport in wood by means of near-infrared hyperspectral imaging coupled with a heat and mass transfer simulation method. *Holzforschung* 76(8):699–710
- Beaulieu J, Dutilleul P (2019) Applications of computed tomography (CT) scanning technology in forest research: a timely update and review. *Can J For Res* 49(10):1173–1188

17. He X, Dawei Q (2013) Density and moisture content forecasting based on X-ray computed tomography. *European Journal of Wood and Wood Products* 71(5):647–652
18. Wang Q, Liu XE, Yang S, Jiang M, Cao J (2019) Non-destructive detection of density and moisture content of heartwood and sapwood based on X-ray computed tomography (X-CT) technology. *Eur J Wood Wood Prod* 77(6):1053–1062
19. CGAL (2023), Computational Geometry Algorithms Library, <https://www.cgal.org>. Accessed 11 May 2023.
20. Tran AP, Yan S, Fang Q (2020) Improving model-based functional near-infrared spectroscopy analysis using mesh-based anatomical and light-transport models. *Neurophotonics* 7(1):015008–015008
21. Si H, Gärtner K (2005) Meshing piecewise linear complexes by constrained Delaunay tetrahedralizations. In: *Proceedings of the 14th international meshing roundtable*. Springer Berlin Heidelberg, pp. 147–163. https://doi.org/10.1007/3-540-29090-7_9
22. Mouchot, N., & Zoulalian, A. (2002). Longitudinal permeability and diffusivity of steam in beech determined with a wicke-kallenbach-cell. *Holzforschung*. <https://doi.org/10.1515/HF.2002.051>
23. Hong JP, Lee JJ, Yeo H, Kim CK, Pang SJ, Oh JK (2016) Parametric study on the capability of three-dimensional finite element analysis (3D-FEA) of compressive behaviour of Douglas fir. *Holzforschung* 70(6):539–546
24. Redman AL, Bailleres H, Gilbert BP, Carr EJ, Turner IW, Perré P (2018) Finite element analysis of stress-related degrade during drying of *Corymbia citriodora* and *Eucalyptus obliqua*. *Wood Sci Technol* 52:67–89
25. Cohen E, Martin T, Kirby RM, Lyche T, Riesenfeld RF (2010) Analysis-aware modeling: Understanding quality considerations in modeling for isogeometric analysis. *Comput Methods Appl Mech Eng* 199(5–8):334–356
26. Schwanninger M, Rodrigues JC, Fackler K (2011) A review of band assignments in near infrared spectra of wood and wood components. *J Near Infrared Spectrosc* 19(5):287–308
27. Englund ET, Thygesen LG, Svensson S, Hill CA (2013) A critical discussion of the physics of wood–water interactions. *Wood Sci Technol* 47:141–161
28. Haloui A, Kouali E, Bouzon J, Vergnaud JM (1994) Process of absorption and desorption of methanol with a 3-dimensional transport through *Picea* wood. *Wood Sci Technol* 28(3):173–184
29. Ouyang B, Yin F, Li Z, Jiang J (2022) Study on the moisture-induced swelling/shrinkage and hysteresis of *Catalpa bungei* wood across the growth ring. *Holzforschung* 76(8):711–721
30. Hailwood AJ, Horrobin S (1946) Absorption of water by polymers: analysis in terms of a simple model. *Trans Faraday Soc* 42:B084–B092
31. Turner IW (1996) A two-dimensional orthotropic model for simulating wood drying processes. *Appl Math Model* 20(1):60–81
32. Carr EJ, Turner IW, Perre P (2013) A dual-scale modeling approach for drying hygroscopic porous media. *Multiscale Model Simul* 11(1):362–384
33. Shi J, Avramidis S (2019) Evolution of wood cell wall nanopore size distribution in the hygroscopic range. *Holzforschung* 73(10):899–910
34. Sun F, Chen K, Tan Y, Peng H, Jiang J, Zhan T, Lyu J (2023) Experimental and numerical assessment of the orthotropic imbibition dynamics of wood. *Wood Mat Sci Eng* 18(2):607–617

Publisher's Note

Springer Nature remains neutral with regard to jurisdictional claims in published maps and institutional affiliations.